International Journal for Housing Science and Its Applications

Publish September 8, 2025. Volume 47, Issue 1 Pages 28-43

https://doi.org/10.70517/ijhsa47103

Study on the Mechanism of Particle Flow and Mass Transfer in a Fluidized Bed Reactor Based on a Multi-Scale Model

Xiaojiao Song[1,*] and Yonghong Guo[1]

[1] Department of Energy and Engineering, Shanxi Institute of Energy, Jinzhong, Shanxi, 030600, China

Corresponding authors: (e-mail: songxiaojiao0930@163.com).

Abstract Aiming at the mixing and separation phenomenon of particles in a gas-solid fluidized bed, a multiscale CFD computational model compatible with a fluidized bed reactor is constructed based on a multiscale model, the gas-phase and solid-phase conservation equations are proposed, and the main structural parameters and non-homogeneous resistance model are determined. Under the condition of considering the bubble mesoscale and the interaction of particle phases in the emulsified phase, a numerical model of mass transfer for gas-solid two-phase flow in the fluidized bed was established, and the complex heat and mass transfer characteristics of two-component particles (quartz sand-rice husk) in the fluidized bed and the parameter influencing law were analyzed. The results show that the flow velocity of solid particles in the fluidized bed reactor increases with the increase of apparent velocity at the inlet gas; the change of mass ratio has a small effect on the transverse velocity of mixed particles, but the effect on the longitudinal velocity is relatively obvious. Meanwhile, it was found that the inlet gas velocity, bed temperature, and operating pressure all had significant effects on the mass transfer efficiency between the gas and solid phases, and a reasonable matching of the external operating conditions is conducive to improving the mass transfer efficiency between the two phases in the fluidized bed reactor.

Index Terms fluidized bed, non-homogeneous drag model, mass transfer, numerical model, two-component particles

I. Introduction

A fluidized bed reactor is a device commonly used for chemical reactions, heat transfer, and mass transfer [1]. It employs the dynamic fluidization of granular material beds to facilitate transfer processes, offering advantages such as rapid reaction rates and high heat and mass transfer efficiency [2], [3]. The mechanisms underlying fluidized bed reactors primarily include the flow characteristics of the fluidized bed, the motion patterns of granular material, and heat and mass transfer during the reaction process [4], [5]. Through the synergistic effects of these mechanisms, fluidized bed reactors can achieve rapid reactions, efficient transport, and stable operation, making them an excellent chemical reaction device [6]-[8]. However, due to the differences in physical properties such as particle diameter and density, the phenomenon of particle mixing and separation occurs in multi-component gas-solid fluidized beds, which directly affects the gas-solid reaction characteristics and fuel conversion rate. Therefore, in-depth research on the separation characteristics of two-component particles in gas-solid fluidized beds will be conducive to obtaining the optimal operating conditions of the system and thereby improving fuel utilization efficiency.

In a fluidized bed reactor, the bed material is dynamically fluidized through fluid dynamics [9]. Within the bed layer, particulate materials are dispersed in the gas flow and move in an irregular manner, forming a flow pattern similar to that of a liquid [10]-[12]. This flow pattern is advantageous for the reaction process as it increases the contact area of the reactants, thereby enhancing reaction rates [13], [14]. The movement patterns of particulate materials are also critical to the reaction process in fluidized bed reactors [15]. Due to collisions and friction between particles, various movement patterns such as rolling, sliding, and colliding occur [16], [17]. These movement patterns and velocities significantly influence both the reaction process and mass transfer process [18]. For example, the dispersion degree and flow velocity of reactants affect reaction rates and mass transfer efficiency, while particle friction and collisions generate heat, influencing reaction temperatures [19]-[21]. Additionally, heat transfer and mass transfer in the reaction process within a fluidized bed reactor are also important mechanisms [22]. Due to the contact between particles and gas flow within the bed layer, heat and mass transfer occur [23]. This transfer mechanism effectively conveys the heat and mass of reaction materials into the bed layer, thereby enhancing reaction rates and transfer efficiency [24], [25].

In this paper, a multi-scale CFD model of fluidized bed reactor is constructed, and a two-fluid model computational framework is adopted to describe the flow structure in the fluidized bed, and a gas-solid traction model is constructed on the

basis of the single-component gas-solid traction model, which is applicable to the two-component mixture fluidized bed system. Finally, the flow and mass transfer characteristics between the solid phase and the gas phase in a fluidized bed with two-component particles are simulated, and the effects of different external operating conditions on the flow and mass transfer characteristics between the two-component particles and the gas are further discussed.

II. Method

With the rapid development of computers, computational fluid dynamics (CFD) has developed a lot of excellent software and mature simulation models, which can be easily carried out for fluidized bed reactor related research [26]. Fluidized bed reactor (FBR) is widely used in industrial production due to its efficient mass and heat transfer performance and good mixing characteristics. In this chapter, a multi-scale CFD computational model equation compatible with fluidized bed reactor will be constructed based on the multi-scale model to propose the mass transfer mechanism of fluidized bed reactor.

II. A. Physical model

II. A. 1) Condition setting

The fluidized bed reactor model used in this simulation is shown in Figure 1. The reactor is 1.5 meters high and 0.2 meters in diameter. It was constructed as a quadrilateral grid using ICEM. The fluidized bed reactor has a velocity inlet at the bottom and a gas outlet set at the top.

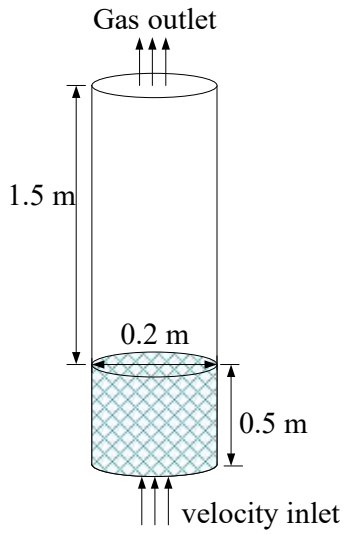

Fluidized bed reactor model

Figure 1: Fluidized bed reactor model

In the reactor cold simulation, the bottom of the reactor is used as the velocity inlet boundary condition. The top is under the free exit boundary condition and the wall is under the non-slip adiabatic condition, and the wall temperature is the ambient temperature. The non-uniform drag model was modeled using a UDF loaded QC-EMMS model with a time step of 0.01 s. The maximum number of iterations for each time step was 20. The maximum number of iterations for each time step was 20.

The unsteady state solution was used and the air inlet was nitrogen. For the thermal state simulation of the reactor, the standard k-ε turbulence model with high computational accuracy and suitable for turbulence simulation was chosen. Throughout the numerical simulation experiments, it was assumed that all solid particles were spherical with smooth outer surface.

II. A. 2) Physical parameters of gas-solid phases

The medium gas-phase medium entering the fluidized bed was nitrogen, and the solid-phase medium was multicomponent particles consisting of quartz gravel and rice husk, whose physical parameters are shown in Table 1.

Table 1: Physical property of gas and solid

Gas phase	Nitrogen		Unit
Density (ρ_s)	1.231		kg/m³
Viscosity (μ_g)	1.795×10^{-5}		Pa·s
Solid phase	Quartz sand particles	Rice husk pellets	
Average particle size(dp)	2840	1520	μm
Particle density (ρ_s)	2500	950	kg/m³
Bulk density (ρ_d)	1350	538	kg/m³

During the entire simulation process, only pyrolysis reactions occurred. Among them, quartz sand particles, as inert bed materials, mainly serve as heat transfer and fluidization media. Rice husk pellets, as biomass raw materials, are the main reactants (cellulose, lignin, etc.). No other catalysts were added during the simulation process. Only the rice husk ash (K, Ca, etc.) in the rice husk particles was used as a natural catalyst.

II. B. Mathematical modeling

II. B. 1) Basic control equations

When modeling a fluidized bed gas-solid fluidization system, a single-phase model only needs to solve the momentum and continuity equations for one phase. However, when analyzing a multi-phase model, it is necessary to introduce multi-phase volume fraction modifications based on the single-phase model and establish additional conservation equations.

(1) Volume fraction

The volume fraction of each phase is denoted by α_p, and each phase satisfies the law of mass conservation. The conservation equations for each phase can be determined using single-phase local transient equilibrium or mixed theory methods.

In the model, the volume V_n of phase p (containing gas phase g and solid phase s) is defined as:

$$V_p = \int_V \alpha_p dV \tag{1}$$

Satisfaction:

$$\sum_{p=1}^{n} \alpha_p = 1 \tag{2}$$

The effective density of phase p is expressed as the product of the volume fraction and the physical density:

$$\hat{\rho}_p = \alpha_p \rho_p \tag{3}$$

(2) Equation of conservation of mass

When there is mass transfer between phases, it is expressed as:

$$\frac{\partial}{\partial t}(\alpha_p \rho_p) + \nabla \cdot (\alpha_p \rho_p \vec{v}_p) = \sum_{p=1}^{n} \dot{m}_{pq} \tag{4}$$

When there is no mass transfer between phases, it is expressed as:

$$\frac{\partial}{\partial t}(\alpha_p \rho_p) + \nabla \cdot (\alpha_p \rho_p \vec{v}_p) = 0 \tag{5}$$

where, $\vec{v}_n$: phase velocity of p, $\dot{m}_{pq}$: mass transfer of phase p and phase q. And it satisfies:

$$\dot{m}_{pq} = -\dot{m}_{pq} \tag{6}$$

$$\dot{m}_{pq} = 0 \tag{7}$$

(3) Momentum Conservation Equation

Gas phase g:

$$\frac{\partial}{\partial t}(\alpha_g\rho_g\vec{v}_g)+\nabla\cdot(\alpha_g\rho_g\vec{v}_g\vec{v}_g)=\nabla\cdot\bar{\bar{\tau}}_g+\alpha_g\rho_g\vec{g}+\alpha_g\rho_g(\vec{F}_g+\vec{F}_{lift,g}+\vec{F}_{lm,g})$$
$$-\alpha_g\nabla p+\sum_{n=1}^{n}(K_{gz^{kn}}(\vec{v}_g-\vec{v}_{z^{kn}})+\dot{m}_{gz^{kn}}\vec{v}_{gz^{kn}}) \tag{8}$$

Solid phase s^{th}:

$$\frac{\partial}{\partial t}(\alpha_s\rho_s\vec{v}_s)+\nabla\cdot(\alpha_s\rho_s\vec{v}_s\vec{v}_s)=-\alpha_s\nabla p-\nabla p_s+\nabla\cdot\bar{\bar{\tau}}_s+\alpha_s\rho_s\bar{g}$$
$$+\alpha_s\rho_s(\vec{F}_s+\vec{F}_{ltf,s}+\vec{F}_{V_{m,s}})+\sum_{l=1}^{n}(K_{lz}(\bar{v}_l-\bar{v}_s)+\dot{m}_{lz}\bar{v}_{lz}) \tag{9}$$

The stress-strain tensor is expressed as:

$$\bar{\bar{\tau}}_s=\alpha_s\mu_s(\nabla\cdot v_s+\nabla\cdot v_s^T)+\alpha_s(\lambda_s-\frac{2}{3}\mu_s)\nabla\cdot v_s\bar{I} \tag{10}$$

In the equation, p_s: particle phase pressure magnitude, μ_s: particle shear viscosity magnitude, λ_ξ: particle volume viscosity magnitude, $\vec{F}_g,\vec{F}_s$: external volume force, $\vec{F}_{lif,g},\vec{F}_{lif,s}$: lift, $\vec{F}_{V_{m,g}},\vec{F}_{V_{m,s}}$: virtual mass force, $K_{gs^{th}},K_{ls}$: gas-solid drag force, solid-solid drag force.

The virtual mass forces of particles in gas-solid flow are much smaller than the inertial forces of particles, so this paper ignores the virtual mass forces. By analogy with the theory of thermal motion of gas molecules, a particle temperature related to the random motion of particles is introduced to describe the kinetic energy of the particle phase. The constitutive equation is used to close the above momentum conservation equations.

II. B. 2) Constitutive equations

This paper uses the particle dynamics theory (KTGF) to describe particle flow and close the above control equations. This theory uses parameters such as "particle viscosity" and "particle pressure" to close the solid corresponding stress and interphase interaction.

(1) Particle temperature

Analogous to the thermodynamic temperature of random molecular thermal motion, the kinetic energy generated by particle motion is expressed using particle temperature:

$$\frac{3}{2}\left[\frac{\partial}{\partial t}(\rho_s\alpha_s\Theta_s)+\nabla\cdot(\rho_s\alpha_s\vec{v}_s\Theta_s)\right]$$
$$=(-p_s\bar{I}+\bar{\bar{\tau}}_s):\nabla\vec{v}_s+\nabla\cdot(k_{\Theta_s}\nabla\Theta_s)-\gamma\Theta_s+\phi_{ls} \tag{11}$$

Among them, $(-p_s\bar{I}+\bar{\bar{\tau}}_s):\nabla\vec{v}_s$: energy generated by the solid state stress tensor, $k_{\Theta_s}\nabla\Theta_s$: energy diffusion ($k_{\Theta s}$ represents the diffusion coefficient), ϕ_{ls}: energy exchange between phases, expressed as:

$$\phi_{ls}=-3K_{ls}\Theta_s \tag{12}$$

$\gamma\Theta_z$: Energy collision dissipation, i.e., the energy dissipation rate caused by solid particle collisions. It can also be given by the Lunetal expression:

$$\gamma_{\Theta m}=\frac{12(1-e_{ss}^2)g_{0,ss}}{d_s\sqrt{\pi}}\rho_s\alpha_s^2\Theta_s^{3/2} \tag{13}$$

(2) Solid pressure

$$p_s=\alpha_s\rho_s\Theta_s+2\rho_s(1+e_{ss})\alpha_s^2g_{0,ss}\Theta_s \tag{14}$$

Among them:

e_{ss}: recovery coefficient of solid-phase collision; $g_{0,ss}$: radial distribution function of solid phase; Θ_s: solid-phase temperature.

(3) Radial distribution function

When the solid phase becomes dense, the particle collision probability is corrected using the radial distribution function, i.e., the dimensionless distance between particles:

$$g_0 = \frac{s + d_p}{s} \tag{15}$$

In the equation, s is the distance between particles. When the solid phase is sparse, $s \to \infty, g_0 \to 1$; when $s \to 0$, $g_0 \to \infty$.

The radial distribution function used in this paper is:

$$g_0 = \left[1 - \left(\frac{\alpha_s}{\alpha_{s,\max}}\right)^{\frac{1}{3}}\right]^{-1} \tag{16}$$

When the number of solid phases is greater than 1, the equation becomes:

$$g_{0,u} = \left[1 - \left(\frac{\alpha_l}{\alpha_{l,\max}}\right)^{\frac{1}{3}}\right]^{-1} \tag{17}$$

$\alpha_{l,}$ is specified in the problem setting and satisfies:

$$g_{0,lm} = \frac{d_m g_{0,\mu} + d_l g_{0,mn}}{d_m + d_l} \tag{18}$$

(4) Solid shear stress

The solid stress tensor is used to describe the momentum exchange generated by the motion and mutual collision of particles, including three parts: collision, movement, and friction:

$$\mu_s = \mu_{s,col} + \mu_{s,kin} + \mu_{s,fr} \tag{19}$$

The collision section is:

$$\mu_{s,col} = \frac{4}{5}\alpha_s \rho_s d_s g_{0,ss}(1 + e_{ss})\left(\frac{\Theta_s}{\pi}\right)^{1/2} \tag{20}$$

The friction parts are:

$$\mu_{s,fr} = \frac{p_s \sin\Phi}{2\sqrt{I_{2D}}} \tag{21}$$

where, $\sin\Phi$: internal friction angle, I_{2D}: second invariant of the shear stress tensor.

The moving part uses the Syamlal expression:

$$\mu_{s,kin} = \frac{\alpha_s \rho_s d_s \sqrt{\Theta_s \pi}}{6(3 - e_{ss})}\left[1 + \frac{2}{5}(1 + e_{ss})(3e_{ss} - 1)\alpha_s g_{0,ss}\right] \tag{22}$$

Another commonly used expression is Gidaspow:

$$\mu_{s,kin} = \frac{10\rho_s d_s \sqrt{\Theta_s \pi}}{96\alpha_s(1 + e_{ss})g_{0,ss}}\left[1 + \frac{4}{5}(1 + e_{ss})\alpha_s g_{0,ss}\right]^2 \tag{23}$$

(5) Solid volume viscosity

The resistance of particles to compression and expansion is the solid bulk viscosity. This paper adopts the form given by Lun:

$$\lambda_s = \frac{4}{3}\alpha_s \rho_s d_s g_{0,ss}(1+e_{ss})\left(\frac{\Theta_s}{\pi}\right)^{1/2} \tag{24}$$

(6) Phase exchange coefficient

The Syamlal-O'Brien symmetric model is used to calculate the interparticle drag coefficient expression as follows:

$$K_{lz} = \frac{3(1+e_{lz})\left(\frac{\pi}{2}+C_{jr,lz}\frac{\pi^2}{8}\right)\alpha_s\rho_s\alpha_l\rho_l(d_l+d_s)^2 g_{0,lz}}{2\pi(\rho_l d_l^3+\rho_s d_s^3)}|\vec{v}_l-\vec{v}_s \tag{25}$$

In the equation, e_{ls}: Solid phase particle recovery coefficient, $C_{fr,ls}$: Solid phase particle friction coefficient, $g_{0,ls}$: Radial distribution function.

II. B. 3) Multi-scale Drag force model

In this paper, the effects of the bubble mesoscale and the interaction of the particulate phase in the emulsified phase on the interphase traction within the bubbling fluidized bed are considered, and a gas-solid traction model applicable to a two-component mixture fluidized bed system is constructed on the basis of the one-component gas-solid traction model [26]. Based on the assumption that no particulate phase exists within the bubble, the average physical properties of the emulsified phase are obtained as:

$$\rho_e = \rho_{p1}\varphi_{ep1} + \rho_{p2}\varphi_{ep2} + \rho_g\varphi_{eg} \tag{26}$$

$$\mu_e = \mu_g[1+2.5(1-\varphi_{ep})+10.05(1-\varphi_{ep})^2+0.00273\exp(16.6+16.6)\varphi_{ep}] \tag{27}$$

$$U_e = (\rho_g U_{ge} + \rho_{p1}U_{ep1} + \rho_{p2}U_{ep2})/\rho_e \tag{28}$$

where ρ_e is the average density of the emulsified phase, kg/m³; ρ_{p1} and ρ_{p2} are the densities of the particles p1 (quartz sand particles) and p2 (rice husk particles) in the emulsified phase, kg/m³, respectively; φ_{ep1} and φ_{ep2} are the volume fractions of particles p1 and p2 in the emulsified phase; μ_e and μ_g are the kinetic viscosities of the emulsified phase and the gas, N-s/m², respectively; φ_{ep} is the total volume fraction of particles in the emulsified phase; U_e is the apparent gas velocity of the emulsion phase, m/s; U_{ge}, U_{ep1}, and U_{ep2} are the apparent gas velocities of the gas phase, particles p1 and p2 in the emulsion phase, m/s.

By introducing an acceleration term to characterize the unsteady properties, the force balance equations for the bubble phase and the particles in the emulsified phase are:

$$\frac{\pi}{8}d_b C_{db}\rho_e U_{eb}^2 = \frac{\pi}{6}(\rho_e-\rho_g)(g+a_b) \tag{29}$$

$$\begin{aligned}&\frac{3}{4}C_{de1}\varphi_{ep1}d_{p1}^{-1}\rho_g U_{ep1}^2+\frac{3}{4}C_{de2}\varphi_{ep2}d_{p2}^{-1}\rho_g U_{ep2}^2\\&\quad=(\rho_{p2}-\rho_g)\varphi_{ep2}(g+a_e)+(\rho_{p1}-\rho_g)\varphi_{ep1}(g+a_e)\end{aligned} \tag{30}$$

Among these, d_b is the bubble diameter, m; C_{db} is the effective drag coefficient of the bubble phase in the traditional drag model; U_{eb} is the apparent gas velocity of the bubble in the emulsion phase, m/s; a_b is the acceleration of the bubble phase, m/s²; C_{de1} and C_{de2} are the effective drag coefficients of particles p1 and p2 in the emulsion phase of the traditional drag model, respectively; a_e is the acceleration of the emulsion phase, m/s².

To characterize the difference in additional mass forces and inertia between the bubble phase and the emulsion phase, their difference is:

$$a_b - a_e = \frac{\sigma^2(\rho_b-\rho_e)g}{C_{de}(1-\varphi_e)\delta_b\rho_e} \tag{31}$$

Among them, ρ_b is the average density of the bubble phase, kg/m³; δ_b is the volume fraction of the bubble phase; σ is the change in the local particle volume fraction concentration.

Based on the definitions of gas and solid volume fractions and the gas-solid mass conservation relationship, the following relationship can be obtained:

$$\begin{cases} \varphi_g = (1-\delta_b)\varphi_e + \delta_b \\ \varphi_e = (1-\delta_b)(\varphi_{ep1} + (\varphi_{ep2}) \end{cases} \tag{32}$$

$$U_g = U_{ge}(1-\delta_b) + \delta_b U_b \tag{33}$$

$$\begin{cases} U_{sp1} = U_{sp1}(1-\delta_b) \\ U_{sp2} = U_{sp2}(1-\delta_b) \end{cases} \tag{34}$$

Among them, U_{sp1} and U_{sp2} are the apparent slip velocities of particles p1 and p2, respectively, in m/s.

For the closed model solution, the minimum energy required to transport suspended particles is set as the particle flow stability criterion, that is:

$$N_s = \frac{1}{(\rho_e - \rho_g)}\left(\frac{3}{4}C_{de1}\frac{\varphi_{ep1}}{d_{p1}}\rho_g U_{ep1}^2 + \frac{3}{4}C_{de2}\frac{\varphi_{ep2}}{d_{p2}}\rho_g U_{ep2}^2\right) \times U_{eg} + f_b U_g (g + a_b) \to \min \tag{35}$$

Among them, f_b is the ratio of the gas volume in the bubble to the total gas volume fraction in the bed.

Based on the solution of the above equation, the relevant local structure parameters can be obtained, and then the drag coefficient expressions for each solid phase of the two-component particles can be obtained:

$$\beta_1 = \frac{\varphi_g^2}{U_{sp1}}\left(\frac{3}{4}C_{de1}\frac{(1-\delta_b)\varphi_{ep1}}{d_{p1}}\rho_g U_{ep1}^2 + \delta_b(\rho_{p1} - \rho_g)\varphi_{ep1}(g + a_b)\right) \tag{36}$$

$$\beta_2 = \frac{\varphi_g^2}{U_{sp2}}\left(\frac{3}{4}C_{de2}\frac{(1-\delta_b)\varphi_{ep2}}{d_{p2}}\rho_g U_{ep2}^2 + \delta_b(\rho_{sp2} - \rho_g)\varphi_{ep2}(g + a_b)\right) \tag{37}$$

Among these, U_{sp1} and U_{sp2} are the apparent slip velocities of the two particles, in m/s.

Based on this, to better characterize the changes in the drag model after considering the bubble mesoscale, the heterogeneity coefficient H_d is introduced, and the calculation formula for the bubble mesoscale drag coefficient becomes:

$$\beta_w = \frac{3}{4}C_d\frac{\varphi_g\varphi_m\rho_g\left|U_g - U_m\right|}{d_{ep}}\varphi_g^{-2.65} \tag{38}$$

$$H_d = \beta_b / \beta_w \tag{39}$$

In the equation, C_d is the drag coefficient of a single particle; β_b and β_w are the bubble mesoscale drag coefficient and the traditional WEN-YU drag coefficient, respectively.

II. B. 4) Mass transfer model

When a gas-solid two-phase fluid flows through a fluidized bed reactor, the total displacement of the fluid is the result of a series of small displacements, each of which is influenced by the combined effects of the average interstitial velocity and random components. Since each random component is independent of the previous one, the entire mass transfer process can be represented by an axial diffusion equation. The specific expression is as follows:

$$\frac{\partial C}{\partial t} = D_e\frac{\partial^2 C}{\partial z^2} - u\frac{\partial C}{\partial z} + R \tag{40}$$

In the equation, C is the component concentration, mol/m^3; z is the axial position, m; u is the average axial gap velocity, m/s; R is the reaction source term; D_e is the axial dispersion coefficient, m^2/s.

The axial diffusion model simulates the axial mixing state of the gas-solid two-phase flow in a fluidized bed reactor by introducing the axial diffusion coefficient. The calculation method of the axial diffusion coefficient is as follows:

$$D_e = 0.73D_m + \frac{0.5u_s d_p}{1 + 9.49D_m / u_s d_p} \tag{41}$$

In the equation, d_p is the average diameter of the component particles, m; u_s is the average interstitial velocity, m/s; D_m is the average molecular diffusion coefficient, m²/s.

The axial diffusion equation is a set of partial differential equations, and the boundary conditions for solving are as follows:

$$-D_e \frac{dC}{dz} = u(C - C_0), z = 0 \tag{42}$$

$$\frac{dC}{dz} = 0, z = L \tag{43}$$

In the axial diffusion model, the reaction process inside the reactor is simulated by introducing a reaction source term R, and the reaction rates of each component are obtained using the Arrhenius equation:

$$k = A \cdot \exp(-\frac{E_a}{RT}) \tag{44}$$

In the equation, A is the pre-exponential factor; E_a is the activation energy, kJ/mol; T is the absolute temperature, K; R is the gas constant, kJ/(mol·K).

III. Results and Analysis

III. A. Analysis of particle flow characteristics in fluidized bed reactors

III. A. 1) Analysis of particle velocity distribution under different fluidization wind speeds

In the simulation experiment, the mass ratio of quartz sand (particle p1) to rice husks (particle p2) is 20:1, where particle p1 serves as the heat transfer medium and particle p2 acts as the catalyst. In the fluidized state of the quartz sand and rice husk mixture, typical simulation results are selected for analysis.

To more intuitively illustrate the influence of the fluidization velocity of the inlet gas on the velocity of two-phase particles in a dense phase bed, this study obtained the distribution of the transverse velocity of the mixed particles under three conditions of fluidization wind speed μ of 0.55 m/s, 0.68 m/s, and 0.84 m/s, as shown in Figure 2. As shown in the figure, as the inlet gas fluidization velocity increases, the average lateral velocity of particles in the dense phase bed increases, and the range of variation in the average lateral velocity of particles also increases, including particles moving to the left and those moving to the right. The increase in wind speed causes the particles in the fluidized bed to move more vigorously, resulting in an increase in lateral velocity, though the magnitude of the increase is not significant.

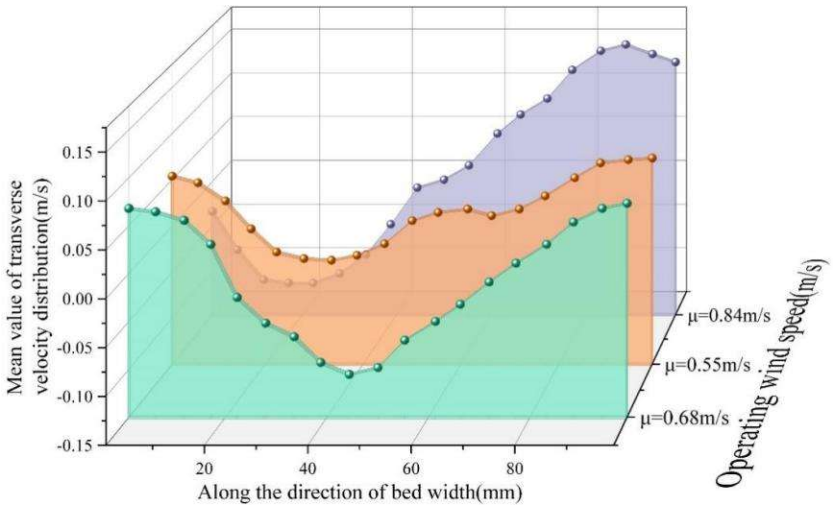

Figure 2: Transverse velocity distribution of particles under different wind speeds

(1) Longitudinal velocity distribution

The longitudinal velocity distribution of particles in the dense phase bed layer at different wind speeds is shown in Figure 3. It can be seen that as the gas flow velocity increases, the upward velocity of the two-phase particles increases, and the number of upward particles also increases. The increase in the longitudinal velocity of particles in the central region is more

pronounced than that in the wall region, and the downward velocity of particles decreases. The results show that as the gas flow velocity increases, particles tend to move upward, with longitudinal movement predominating.

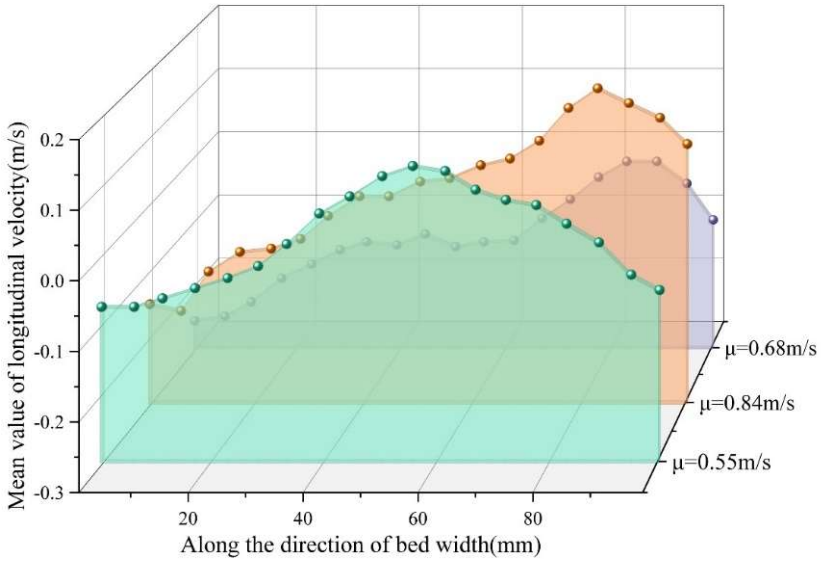

Figure 3: Longitudinal velocity distribution of particles under different wind speeds

(2) Velocity distribution

The overall velocity distribution of particles in the dense phase bed under different gas flow velocities is shown in Figure 4. Overall, the fluidization velocity of the mixed particles increases gradually with the increase in fluidization airflow. As the fluidization airflow increases, the overall velocity of the particles also increases, and the number of particles in the high-velocity core region also increases. At the wall, some particles even have higher velocities than those in the core region. This may be due to the increased height of the particles after being dispersed, resulting in a higher falling velocity during the descent, or it may be caused by the uncertainty in the movement of bubbles within the fluidized bed.

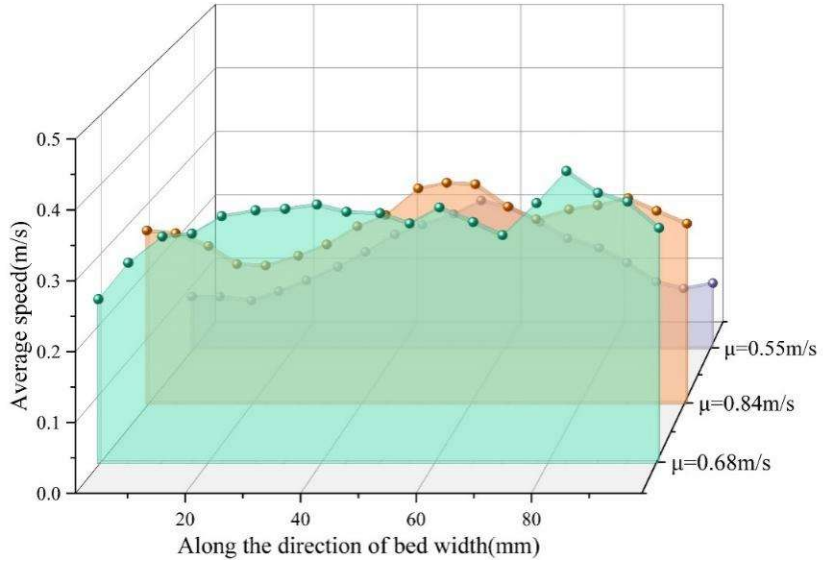

Figure 4: Particle velocity distribution under different wind speed

III. A. 2) Analysis of the effect of different mass ratios on particle flow fields

When the operating wind speed is 0.68 m/s, the particle velocity distribution is analyzed under different mass ratios of quartz sand particles to rice husk particles (20:1, 30:1, and 40:1), with representative simulation results selected for analysis.

(1) Lateral velocity distribution

The lateral velocity distribution of the gas-tight bed layer for quartz sand and rice husk particles at different mass ratios is shown in Figure 5. As can be seen from the figure, the lateral velocity values of the particles slightly increase as the mass ratio of the mixed particles decreases, and the change in mass ratio has a mild effect on the lateral velocity of the mixed particles. Near the transition zone, the lateral velocity remains high, indicating a region of intense motion. Near the central and wall regions, the lateral velocity is lower. In studies of wind speed convection fields, it has been found that changes in gas flow velocity have a significant impact on the convection field. However, when the gas flow velocity remains unchanged, changes in the concentration of biomass powder in the mixed particles do not have a noticeable effect on the lateral velocity.

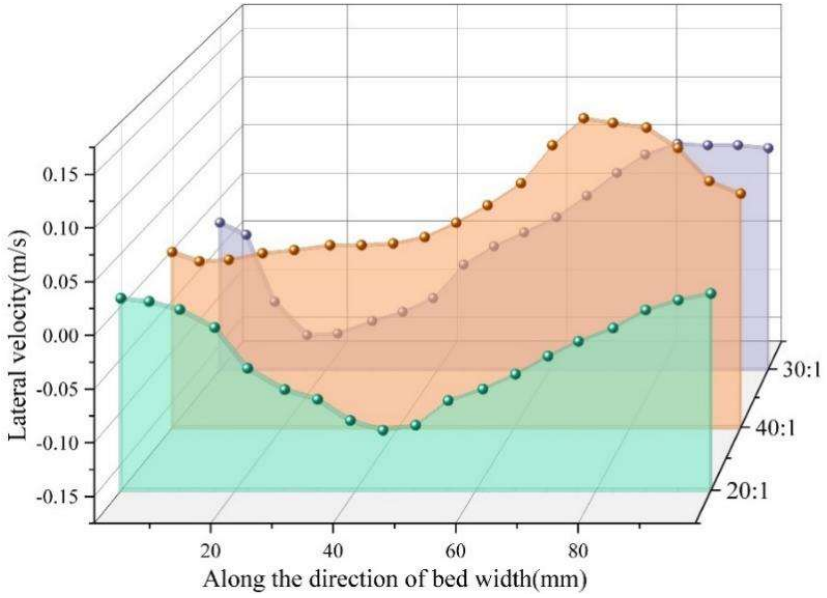

Figure 5: The transverse velocity distribution under different mass ratios

(2) Longitudinal velocity

The longitudinal velocity distribution of dense-phase beds with different mass ratios of quartz sand and rice husk particles is shown in Figure 6. The effect of different mass ratios of mixed particles on longitudinal velocity is quite noticeable, especially for particles in the central region. Bubbles push most of the upper particles upward. As the mass ratio decreases, the number of upward-moving particles and their longitudinal velocity both increase significantly, resulting in a more dispersed longitudinal velocity distribution. Particles in the transition zone and wall regions primarily move downward, with a more gradual increase in longitudinal velocity, forming a ring-core motion pattern relative to the central region.

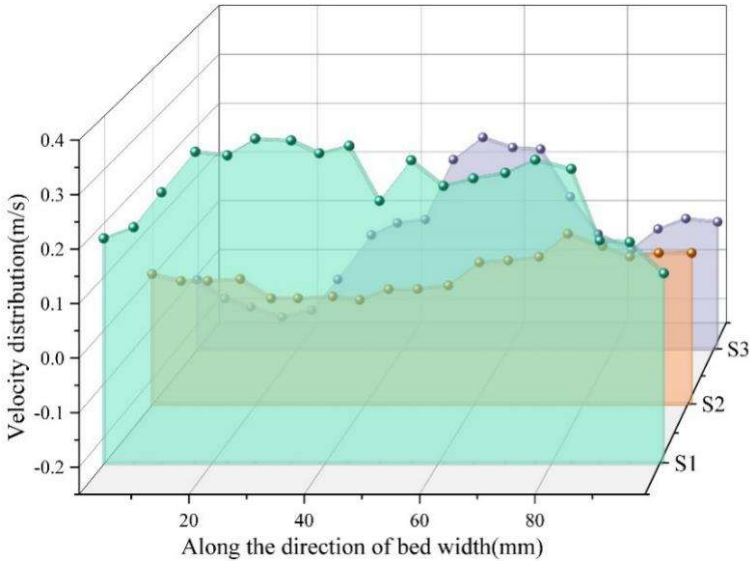

Figure 6: Longitudinal velocity distribution at different mass ratios

Since the density of rice husk particles is much lower than that of quartz sand particles, the velocity gained by rice husk particles when bubbles burst is significantly greater than that of quartz sand particles. Collisions between mixed particles intensify, and their proportion in the mixed particles increases, which causes the overall longitudinal velocity of the mixed particles to increase and leads to an increase in the number of upward-moving particles. The mean value of the longitudinal velocity distribution increases as the mass ratio of quartz sand to rice husk particles in the mixed particles decreases.

(3) Velocity distribution

The overall velocity distribution of the dense phase bed under different mass ratios is shown in Figure 7. It can be seen that as the mass ratio of mixed particles decreases, the proportion of rice husk particles increases, and the particle velocity distribution becomes more dispersed. For mass ratios of 20:1, 30:1, and 40:1, the mean velocities are 0.32 m/s, 0.23 m/s, and 0.21 m/s, respectively. It is evident that as the mixed mass ratio of quartz sand and rice husk particles decreases, the average velocity also increases. Among these, the change in particle velocity in the central region is more pronounced.

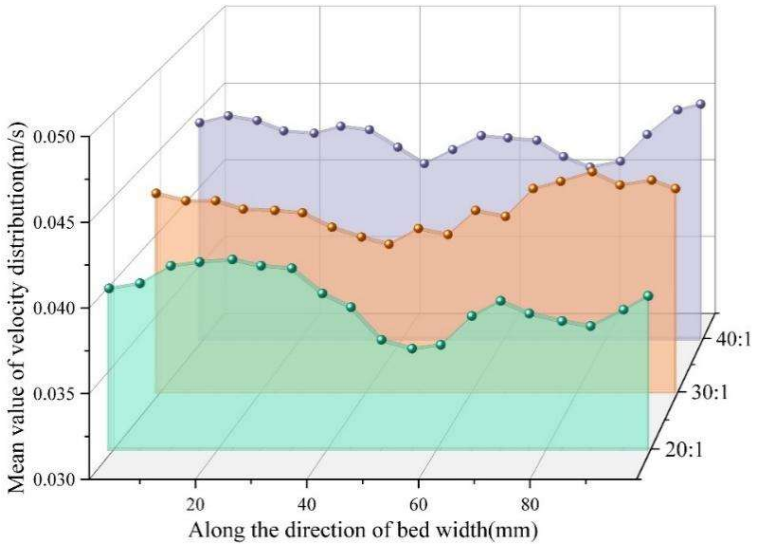

Figure 7: Velocity distribution under different mass ratios

III. B. Analysis of mass transfer characteristics in fluidized beds

III. B. 1) Boundary conditions

Based on the fluidized bed reactor model shown in Figure 1, this paper uses mass flow inlet and pressure outlet boundaries in numerical calculations, symmetric boundary conditions on the symmetric plane, and constant wall temperature boundaries internally. The temperature is taken as the saturated steam temperature at 4.1 MPa, i.e., ti = 525 K. The gas flow at the wall surface uses no-slip boundary conditions and standard wall functions. The particle size distribution of the mixed particles is calculated using the Rosin-Rammler distribution, as shown in Table 2. The detailed operating parameters for the gas and mixed particles are listed in Table 3.

Table 2: Particle size distribution of Mixed particles

Diameter designation	Particle size (μm)
Minimum diameter	1.452
Maximum diameter	481.65
Average diameter of mixed particles	227.34

Table 3: Operating Parameters of gas and Mixed Particles in fluidized bed 4

Boundary conditions	Value	Unit
Initial inlet gas velocity	0.05	m/s
Initial bed temperature	298	K
Initial operating pressure	4	MPa

III. B. 2) Grid partitioning and model solution

This paper utilizes Gambit software to construct a fluidized bed reactor model. Additionally, to reasonably select the number of grids for calculation, this paper verifies the mesh independence and examines the impact of different mesh partitioning scales on the calculation results. As shown in Table 4, with the increase in the number of meshes, the heat transfer coefficient gradually increases, and the rate of increase gradually decreases, i.e., the relative error decreases. Therefore, considering the accuracy and speed of numerical calculations, the appropriate number of meshes is finally determined to be 534,650.

Table 4: Grid independent check

Number of grids	Heat transfer coefficient (W/(m²·K))	Relative error
105050	95.37	-
324500	99.14	2.84%
534650	100.52	1.83%
743200	101.01	0.75%

The control equations to be solved in the numerical calculations of this paper primarily include the Realizable k-ε turbulence equations, particle motion equations, and energy equations. Ansys Fluent 18.0 was used to solve the control equations in a non-steady state, and the independence of the time step was verified, with a final value of 0.1 s. The specific data is shown in Table 5. The numerical calculations employ the control volume method, integrating the differential equations of each mathematical model within a unit control volume to obtain the corresponding integral equations. These integral equations are then discretized into a series of algebraic equations and solved iteratively. Pressure coupling is solved using the SIMPLE semi-implicit method and the PRESTO discretization method, based on mass, momentum, and energy transfer equations.

Table 5: Time step independence check

Time step	Heat transfer coefficient (W/(m²·K))	Relative error
10	100.2033	-
1	101.0684	2.79%
0.1	101.0937	1.81%
0.01	101.1105	0.73%

Additionally, the relaxation factors for variables such as pressure, density, volume force, momentum, turbulent kinetic energy, turbulent dissipation rate, energy, and discrete coordinates are set to 0.3, 1, 1, 0.7, 0.8, 0.8, 0.8, and 0.8, respectively. The overall calculation is conducted in different stages. First, the unsteady gas-phase flow field and temperature field are calculated. Once the calculation has stabilized, two-phase particles are introduced into the calculation.

III. B. 3) Analysis of simulation results

(1) Effect of inlet gas flow velocity on mass transfer characteristics

The inlet gas flow velocity within the fluidized bed has a significant correlation with gas-solid heat transfer characteristics. Figure 8 simulates the variation of the non-uniformity coefficient with bed porosity when the inlet gas flow rate is 0.05 m/s, 0.07 m/s, 0.09 m/s, 0.11 m/s, and 0.13 m/s, and the average diameter of the mixed particles is 227.34 μm. As can be clearly observed from the figure, the heterogeneity coefficient of the mixed particles increases with an increase in bed porosity. As the apparent inlet gas velocity increases, the heterogeneity coefficient of rice husk particles gradually decreases, indicating that smaller porosity and larger inlet apparent velocity lead to a greater influence of bubbles on mesoscale drag forces, resulting in more pronounced bed heterogeneity characteristics.

Figure 9 shows the variation in gas mass fraction at the outlet of the fluidized bed over time under five different apparent gas velocity conditions. As can be clearly observed from the figure, when the mass fraction of mixed particles is constant, the gas concentration at the outlet of the fluidized bed increases gradually as the apparent inlet gas velocity increases. This is primarily because the set inlet apparent velocity is slightly greater than the minimum fluidization velocity of the fluidized bed, causing the bed to remain in a bubbling fluidized state. As the inlet apparent velocity increases, bubbles will aggregate and grow to a certain extent, penetrating through the particle layer. This reduces the contact time and contact area between gas and particles, resulting in a significant amount of gas being blown out of the fluidized bed.

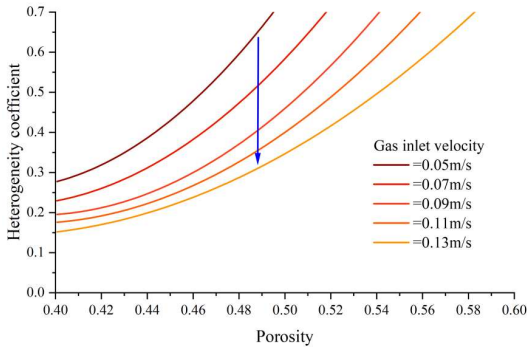

Figure 8: The variation of the heterogeneity coefficient under different inlet airflow velocities

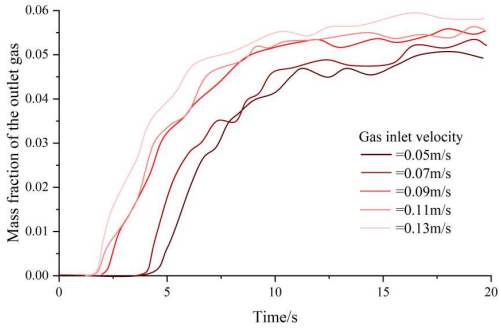

Figure 9: Changes in the mass fraction of the outlet gas under different inlet velocity conditions

When t = 10 s, the distribution cloud map of quartz sand particles and rice husk particles is shown in Figure 10. As can be seen from the figure, as the apparent inlet velocity increases, the bed expansion height of quartz sand particles gradually increases, bubbles in the bed become more pronounced, and the volume fraction of bubbles also gradually increases. Rice husk particles are also gradually lifted as the expansion height of the quartz sand particle bed increases. Additionally, as the inlet gas velocity increases, the separation efficiency between quartz sand particles and rice husk particles gradually decreases. Due to the passage of bubbles through the rice husk particle layer, quartz sand particles begin to aggregate as the velocity increases, and the degree of aggregation gradually intensifies. Based on the above results, it is found that as the inlet gas flow velocity increases, the separation degree between the mixed particles gradually weakens. Therefore, reasonably matching the inlet gas velocity is a key measure to achieve efficient separation of two-component particles and an effective method to control mass transfer between gas and solid phases.

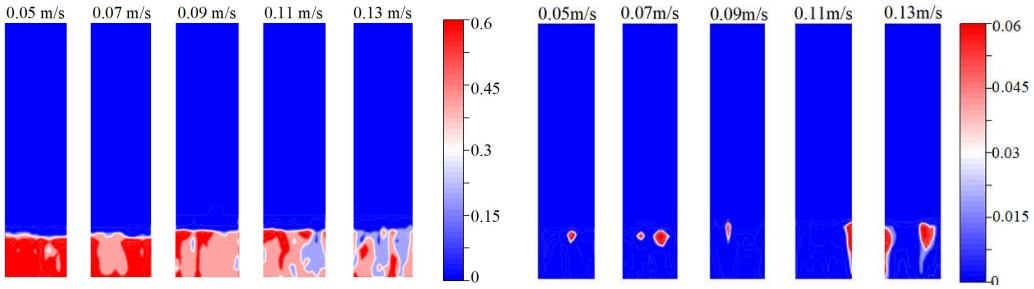

(a) Quartz sand particles (b) Rice husk pellets

Figure 10: Cloud map of the distribution of mixed particle concentrations at different inlet gas velocities

(2) Effect of bed temperature on mass transfer characteristics

Fluidized bed reactors sometimes operate at high temperatures. At an initial inlet gas velocity of 0.05 m/s, the bed temperatures were set to 298 (initial value), 398, and 498 K. The effect of bed temperature at t = 10 s on the instantaneous particle concentration distribution cloud map is shown in Figure 11. As shown in Figure 11, as the bed temperature increases, the gas viscosity increases, solid particles tend to agglomerate, and the degree of two-phase particle separation gradually weakens.

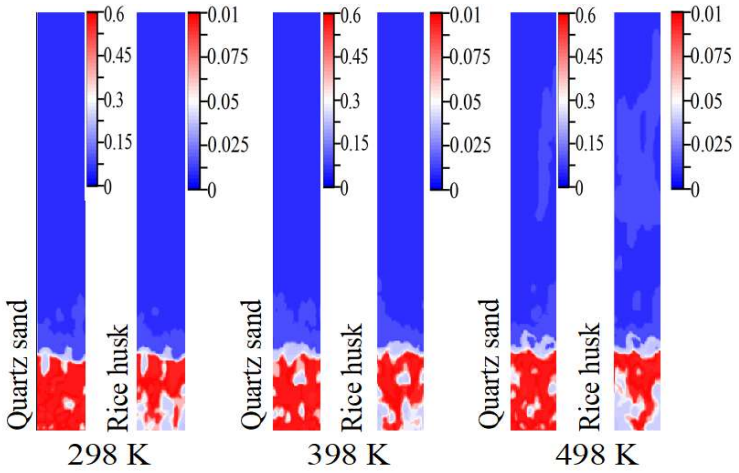

Figure 11: Effect of bed temperature on instantaneous particle concentration distribution nephogram

The effect of bed temperature on the particle mixing index is shown in Figure 12. As shown in Figure 12, as the bed temperature increases, the mixing index gradually increases, and the separation efficiency gradually decreases. This is primarily due to the fact that as the bed temperature increases, the gas viscosity increases, the density decreases, resulting in a decrease in the gas-solid drag coefficient, and ultimately leading to a decrease in the non-homogeneous coefficient. The non-homogeneous coefficients of the two-phase particles decrease at different rates, causing the difference between them to gradually decrease. Additionally, the increase in gas viscosity makes particles more prone to adhesion and less separable. Therefore, in addition to modifying particle properties and external operating conditions, appropriately reducing the bed temperature can also enhance particle separation efficiency.

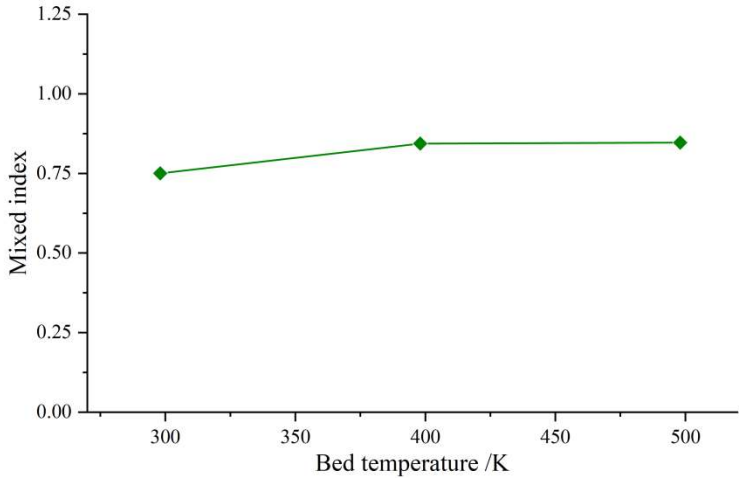

Figure 12: Effect of bed temperature on particle mixing index

(3) Effect of operating pressure on mass transfer characteristics

Based on the initial values of inlet gas flow velocity and bed temperature, and keeping all other operating parameters constant, calculations were performed by varying the operating pressure within the fluidized bed (4 MPa, 4.3 MPa, 4.6 MPa, 4.9 MPa, 5.2 MPa). The specific results are shown in Figure 13. As can be seen, as the operating pressure within the fluidized bed increases, the average thickness of the particle layer gradually decreases. This is because, when the inlet gas mass flow rate remains constant, an increase in operating pressure causes the density of the inlet gas to increase, thereby reducing the inlet gas flow velocity within the fluidized bed, and consequently decreasing particle deposition. The thermal resistance decreases gradually as the particle deposition thickness decreases, and its trend is consistent with that of the particle deposition thickness. As the operating pressure increases, the inlet gas flow velocity decreases gradually, which reduces the convective heat transfer coefficient of the particle layer in the fluidized bed and also slows down the temperature decrease of the gas in the fluidized bed, resulting in an increased temperature difference between the gas layer and the particle layer, thereby enhancing the heat transfer coefficient between the gas and solid phases.

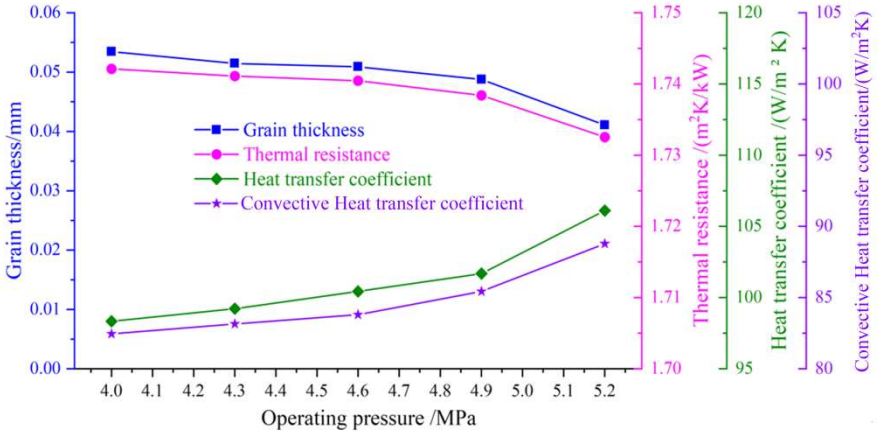

Figure 13: Deposition and heat transfer characteristics at different operating pressures

The results of the changes in the heat transfer coefficient within the fluidized bed under different operating pressures are shown in Figure 14. From the specific trend of the changes, it can be observed that the decrease in the convective heat transfer coefficient is not as significant as the increase in the radiative heat transfer coefficient. Therefore, under the combined influence of convection and radiation, the heat transfer coefficient gradually increases with the rise in operating pressure. Due to the presence of thermal resistance, the heat transfer coefficient is numerically lower than the heat transfer coefficient, and its trend aligns with that of the heat transfer coefficient. This is because thermal resistance decreases gradually with increasing operating pressure, leading to an increase in the heat transfer coefficient. Therefore, the heat transfer coefficient is influenced by both factors and also increases gradually with increasing operating pressure.

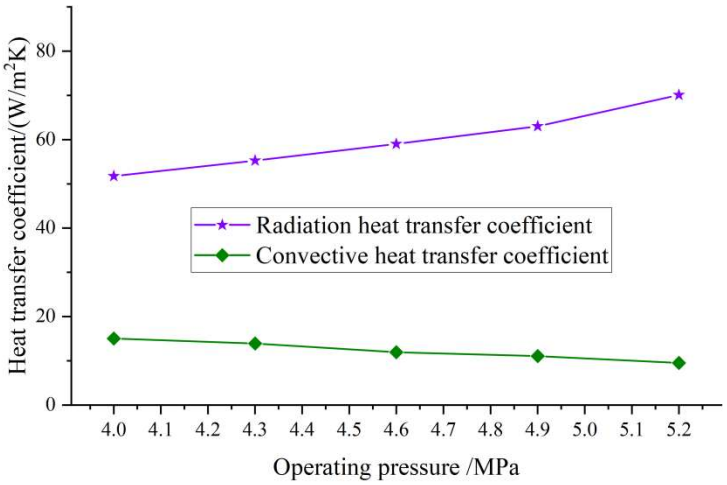

Figure 14: The variation of heat transfer coefficient under different operating pressures

IV. Conclusion

A two-component gas-solid drag force model was established using bubbles as the mesoscale, and the flow and mass transfer characteristics of two-component particles were simulated in a fluidized bed reactor. The conclusions are summarized as follows:

(1) The flow velocity of solid particles in the fluidized bed reactor increases with the increase in the apparent velocity at the gas inlet; changes in the mass ratio have little effect on the lateral velocity of the mixed particles, but have a relatively significant effect on the longitudinal velocity.

(2) As the inlet gas velocity increases, the heterogeneity coefficient of rice husk particles gradually decreases, and bubbles aggregate to some extent, penetrating through the particle layer. This reduces the contact time and contact area between gas and particles, leading to a significant amount of gas being blown out of the fluidized bed and weakening the separation degree between mixed particles. Additionally, bed temperature and operating pressure also affect mass transfer efficiency within the fluidized bed. Therefore, in practical applications, external operating conditions should be appropriately matched to enhance heat and mass transfer efficiency within the fluidized bed.

Funding

This research was supported by the Shanxi Institute of Energy Institutional-Level Scientific Research Fund Project: "Study on Flow and Mass Transfer Characteristics of Multicomponent Particles in Fluidized Bed Reactors" (Project No. ZY-2023022).

References

[1] Rowe, P. N., & Yates, J. G. (2020). Fluidized-bed reactors. In Chemical reaction and reactor engineering (pp. 441-498). CRC Press.
[2] Bello, M. M., Raman, A. A. A., & Purushothaman, M. (2017). Applications of fluidized bed reactors in wastewater treatment–a review of the major design and operational parameters. Journal of Cleaner Production, 141, 1492-1514.
[3] Suleiman, Y., Ibrahim, H., Anyakora, N. V., Mohammed, F., Abubakar, A., Aderemi, B. O., & Okonkwo, P. C. (2013). Design and fabrication of fluidized-bed reactor. International Journal of Engineering and Computer Science, 2(5), 1595-1605.
[4] Leion, H., Frick, V., & Hildor, F. (2018). Experimental method and setup for laboratory fluidized bed reactor testing. Energies, 11(10), 2505.
[5] Mathekga, H. I., Oboirien, B. O., & North, B. C. (2016). A review of oxy–fuel combustion in fluidized bed reactors. International Journal of Energy Research, 40(7), 878-902.
[6] Zhu, Q., Hao, W., Tao, J., Huang, Q., & Yang, C. (2021). State dependence of magnetized fluidized bed reactor on operation mode. Chemical Engineering Journal, 407, 127211.
[7] Khadilkar, A., Rozelle, P. L., & Pisupati, S. V. (2014). Models of agglomerate growth in fluidized bed reactors: Critical review, status and applications. Powder Technology, 264, 216-228.
[8] Akbari, V., Borhani, T. N. G., Shamiri, A., & Shafeeyan, M. S. (2024). Computational fluid dynamics modeling of gas-solid fluidized bed reactor: Influence of numerical and operating parameters. Experimental and Computational Multiphase Flow, 6(2), 85-125.
[9] Silva, G. G., Jiménez, N. P., & Salazar, O. F. (2012). Fluid Dynamics of Gas-Solid Fluidized Beds. Advanced Fluid Dynamics, 39.
[10] Haus, J., Hartge, E. U., Heinrich, S., & Werther, J. (2017). Dynamic flowsheet simulation of gas and solids flows in a system of coupled fluidized bed reactors for chemical looping combustion. Powder technology, 316, 628-640.
[11] Sun, Z., & Zhu, J. (2022). Comparison of flow dynamics and reactor performance in gas-solids circulating turbulent fluidized bed with other fluidized beds across regimes. Chemical Engineering Journal, 446, 137313.
[12] Leckner, B. (2022). Fluid dynamic regimes in circulating fluidized bed boilers—A mini-review. Chemical Engineering Science, 247, 117089.
[13] Khan, M. J. H., Hussain, M. A., Mansourpour, Z., Mostoufi, N., Ghasem, N. M., & Abdullah, E. C. (2014). CFD simulation of fluidized bed reactors for polyolefin production–A review. Journal of Industrial and Engineering Chemistry, 20(6), 3919-3946.
[14] Pan, H., Chen, X. Z., Liang, X. F., Zhu, L. T., & Luo, Z. H. (2016). CFD simulations of gas–liquid–solid flow in fluidized bed reactors—A review. Powder Technology, 299, 235-258.
[15] Blaszczuk, A., Zylka, A., & Leszczynski, J. (2016). Simulation of mass balance behavior in a large-scale circulating fluidized bed reactor. Particuology, 25, 51-58.
[16] Bellan, S., Gokon, N., Matsubara, K., Cho, H. S., & Kodama, T. (2018). Numerical and experimental study on granular flow and heat transfer characteristics of directly-irradiated fluidized bed reactor for solar gasification. International Journal of Hydrogen Energy, 43(34), 16443-16457.
[17] Qin, K., Thunman, H., & Leckner, B. (2017). Mass transfer under segregation conditions in fluidized beds. Fuel, 195, 105-112.
[18] Lim, E. W. C. (2013). Mixing behaviors of granular materials in gas fluidized beds with electrostatic effects. Industrial & Engineering Chemistry Research, 52(45), 15863-15873.
[19] Montellà, E. P., Toraldo, M., Chareyre, B., & Sibille, L. (2016). Localized fluidization in granular materials: Theoretical and numerical study. Physical Review E, 94(5), 052905.
[20] Yan, L., Cao, Y., Zhou, H., & He, B. (2018). Investigation on biomass steam gasification in a dual fluidized bed reactor with the granular kinetic theory. Bioresource technology, 269, 384-392.
[21] Wang, S., Luo, K., Hu, C., Sun, L., & Fan, J. (2018). Impact of operating parameters on biomass gasification in a fluidized bed reactor: An Eulerian-Lagrangian approach. Powder Technology, 333, 304-316.
[22] Lu, Y., Kang, P., Yang, L., Hu, X. E., Chen, H., Zhang, R., ... & Yang, Y. (2020). Multi-scale characteristics and gas-solid interaction among multiple beds in a dual circulating fluidized bed reactor system. Chemical Engineering Journal, 385, 123715.
[23] Li, Z., Janssen, T. C. E., Buist, K. A., Deen, N. G., van Sint Annaland, M., & Kuipers, J. A. M. (2017). Experimental and simulation study of heat transfer in fluidized beds with heat production. Chemical engineering journal, 317, 242-257.
[24] Eder, C., Hofer, G., & Pröll, T. (2021). Wall-to-bed heat transfer in bubbling fluidized bed reactors with an immersed heat exchanger and continuous particle exchange. Industrial & Engineering Chemistry Research, 60(19), 7417-7428.
[25] Abdelmotalib, H. M., Youssef, M. A., Hassan, A. A., Youn, S. B., & Im, I. T. (2015). Heat transfer process in gas–solid fluidized bed combustors: A review. International Journal of Heat and Mass Transfer, 89, 567-575.
[26] Ahmad Nouman, Deng Jianqiang & Adnan Muhammad. (2022). Numerical investigation for the suitable choice of bubble diameter correlation for EMMS/bubbling drag model. Chinese Journal of Chemical Engineering,47,254-270.